Chapter 7
Mathematics of Neutron Imaging

K.W. Tobin, P.R. Bingham, and J. Gregor

Abstract Imaging with neutrons at macro-world scales (e.g., $>10\,\mu m$) requires particular understanding of the non-diffracting or refracting interactions that these electrically neutral particles have with their environment. While image formation with neutrons shares some commonality with other radiation sources such as X-rays and gamma rays, neutrons provide complementary interaction mechanisms to these techniques that can uniquely probe materials and structure. Neutron sources are also historically fraught with issues regarding low source intensities, challenging beam configurations and resolution limitations that are all closely linked. In this chapter we will present a mathematical construct and methods compatible with the design and characterization of radiography systems for volumetric imaging. We begin with a review of neutron image formation, provide resolution analysis concepts and methods for both the design and the characterization of radiography systems, and conclude with a review and discussion of volumetric reconstruction techniques using analytic or iterative computed tomography algorithms.

Keywords Neutron radiography · Computed tomography · Modeling · Resolution · Contrast

7.1 Introduction

Neutron imaging has long been known to provide complementary, nondestructive imaging capabilities to X-ray and gamma-ray imaging methods [3]. Today, neutron imaging with conventional reactor-based sources enables the interrogation of complex, multicomponent systems for many applications, such as nuclear material nondestructive testing [9], characterizing flight control surfaces on aircraft [4], testing heat transfer in porous materials [30], examining

K.W. Tobin (✉)
Image Science and Machine Vision Group, Oak Ridge National Laboratory, Oak Ridge, Tennessee 37831-6075
e-mail: tobinkwjr@ornl.gov

I.S. Anderson et al. (eds.), *Neutron Imaging and Applications*, Neutron Scattering Applications and Techniques, DOI 10.1007/978-0-387-78693-3_7,

heat exchanger systems [2, 10], development of hydrogen fuel cells (Chapter 11), inspection of cultural heritage objects (Chapter 13), and interrogating biological systems [28]. Newer, intense sources of neutrons from spallation facilities are providing the potential to interrogate time and energy-dependent phenomena as well. Therefore, a mathematical representation of the neutron image formation process can provide insight into the potential application of time- and energy-dependent, volumetric radiography to the characterization and quantitation of complex material structures.

The mathematics of neutron imaging is similar to that of other non destructive methods that use non-refracting or diffracting radiation to interrogate materials or composites of materials [3]. Figure 7.1 represents the basic elements of a generic neutron radiography system beginning with a source of neutrons, beam conditioning and shaping, neutron conversion and detection, and sampling and signal generation.

For the purposes of this discussion, neutron image formation will be treated as an encoding of the material characteristics of a three-dimensional (3D) object projected onto a two-dimensional (2D) detection array, typically comprising a converter followed by an imaging sensor as described in Chapter 5. Material characteristics of the object are represented by the total macroscopic interaction cross-section, Σ_T, which is a sum of the absorption and scattering cross-sections, $\Sigma_T = \Sigma_a + \Sigma_s$ (i.e., ignoring the potential for neutron capture and fission cross-sections in some materials). The interaction of the neutron beam, ϕ_o, with the 3D object produces a total 2D field at the converter plane, ϕ_T, that can be decomposed into the uncollided flux, ϕ_u, and the scattered flux, ϕ_s, as $\phi_T = \phi_u + \phi_s$. The uncollided flux arises from neutrons that arrive at the converter plane unperturbed by the imaged object while the scattered flux considers only neutrons that have been scattered by the object toward the converter plane.

To understand the dependencies of the scattered flux on the image formation process, we introduce a buildup factor [20, 24] defined as $B = \phi_T/\phi_u = 1 + \phi_s/\phi_u$. Rearranging to solve for ϕ_T, we can represent the total flux at the converter plane as $\phi_T = B\phi_u$, i.e., a multiplicative build up of the uncollided flux due to object scattering. This is represented using the well-known neutron

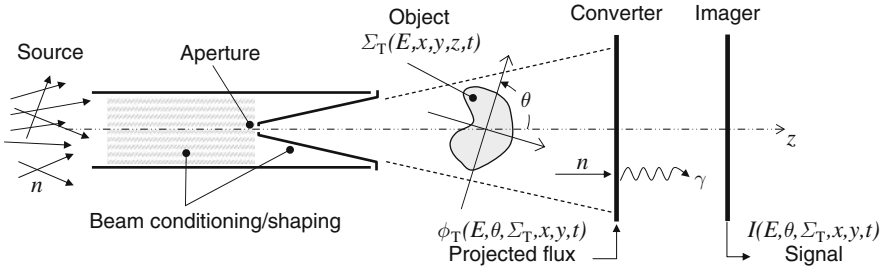

Fig. 7.1 Basic elements of a neutron radiography-imaging environment. A source of neutron is typically shaped and collimated, interacts with the material constituents of a 3D object and is projected onto a 2D imaging array

attenuation law as $\phi_T = \phi_o B \exp\{-\int \Sigma_T dz\}$, or with space-, time-, and energy-dependencies as,

$$\phi_T(E,\theta,\Sigma_T,x,y,t) = \phi_o(E,x,y,t)B(E,\theta,\Sigma_s,x,y,t)e^{-\int \Sigma_T(E,x,y,t,z)dz} \quad (7.1)$$

where x and y are spatial position in the plane perpendicular to the ray from source to detector, z represents position along ray from source to detector and E is the neutron energy. In this relationship, θ corresponds to the angular orientation of the object under test (Fig. 7.1) and is included as a prelude to later discussions regarding volumetric reconstruction from projections. Also note that the buildup factor is a value $B \geq 1$. It is functionally dependent on the material composition and geometry presented by the object under test and is therefore difficult to predict or accommodate under typical radiographic conditions. Buildup can be significant for materials containing, e.g., H, Si, Ni, Cu, and other highly scattering metals, and should be considered a source of error in quantitative analysis. For example, imaging geometries that move the object away from the detection plane can reduce the number of neutrons scattered into the detector, but this may also reduce the system resolution due to the characteristics of the beam aperture. The beam aperture and length is typically characterized by the L/D ratio, where L denotes the distance from the aperture to the object and D is the diameter of the aperture. This effect will be detailed further in Section 7.2.

Note that a primary goal of image analysis can be formulated as one of measuring the interaction cross-section of the materials in the imaged object, $\Sigma_T(E,x,y,z)$. Direct measurement of Σ_T, for example, provides indirect information regarding other material properties since $\Sigma = N\sigma = \sigma\rho N_A/M$, where σ is the microscopic cross-section, N is the number of atoms per cm^2, ρ is the material density, N_A is Avagadro's number, and M is the atomic weight [25].

The electronic signal produced by the system is further impacted beyond the geometry effects of L/D by the response of the converter, optical components, and sensor (e.g., a charge-coupled device, CCD). Making the practical assumption of a linear shift invariant (LSI) system [14], we can describe the time-, space-, and energy-dependent 2D electronic image, I, in terms of a convolution of the modulated (by the object) neutron field at the converter, ϕ_T, with a system impulse response function, h, to give,

$$\begin{aligned} I(E,\theta,\Sigma_T,x,y,t) &= \int\int \phi_T(E,\theta,\Sigma_T,\alpha,\beta,t)h(x-\alpha,y-\beta)d\alpha d\beta \\ &= \phi_T(E,\theta,\Sigma_T,x,y,t) \times h(x,y) \end{aligned} \quad (7.2)$$

In Section 7.2 we will model and analyze the impulse response of a radiography system to estimate system design resolution and characterize resolution of an existing radiography system through empirical means. In Section 7.3 we will describe considerations and methods required to perform volumetric reconstruction and estimation of Σ_T using projection data and computed tomography based on both analytic and iterative techniques.

7.2 Neutron Image Formation and Resolution Analysis

In this section, we will describe the image formation characteristics of a neutron radiography system from both a modeling and an empirical perspective. A model of resolution is important when designing a system to ensure that realistic resolution goals can be established and achieved. Once a system is operational, an empirical methodology is required to verify performance.

7.2.1 Resolution Modeling

For modeling purposes, Fig. 7.2 represents an idealized radiography system containing the basic elements described earlier in Fig. 7.1. The goal of a resolution model is to understand the impact of various system components on signal degradation. For this analysis we will neglect the impact of electron noise and counting statistics, and focus instead on the effects of the neutron aperture, D, the optical diffusion response of a scintillator, δ, the optical component, and sampling at the sensor, Δs (e.g., by a CCD camera).

The effects of these system elements are fundamentally described through the system impulse response, $h(x)$, introduced in Eq. (7.2), which will be expressed as 1D for this discussion. In an LSI system, the response, $I(x)$, is a convolution of the real-world signal, $\phi_T(x)$ in our case, with an impulse function, $h(x)$, as $I(x) = \phi_T(x)*h(x)$. The total impulse response can be decomposed into elements representing the major components of the system. For our case, based on Fig. 7.2, $h(x) = h_D(x)*h_\delta(x)*h_{CCD}(x)$, corresponding to the neutron beam aperture, scintillator, and CCD sensor, respectively. We model these components of the system using idealized functions for the physical neutron beam aperture, converter optical diffusion, and sensor sampling,

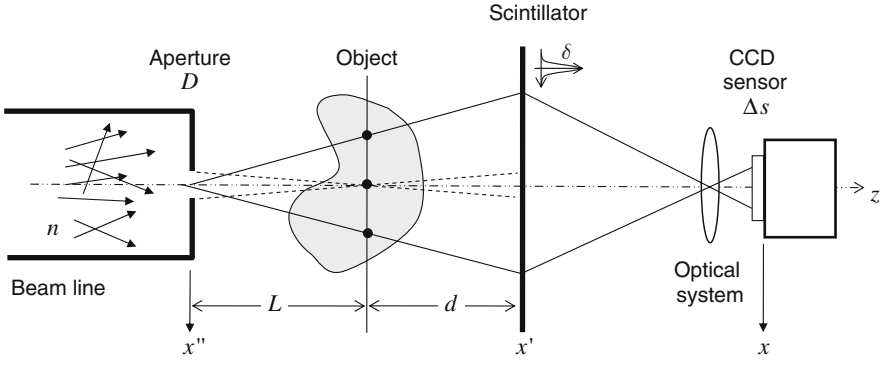

Fig. 7.2 Representation of a basic radiographic image formation system used to estimate resolution performance during the design stage. Model accounts for geometry, aperture size, scintillator resolution, and optical system resolution

$$h_{\mathrm{D}}(x'') = \mathrm{rect}\left(\frac{x''}{D}\right), h_{\sigma}(x') = \mathrm{Gauss}\left(\frac{x'}{\delta}\right), h_{\mathrm{CCD}}(x) = \mathrm{rect}\left(\frac{x}{\Delta s}\right) \quad , \qquad (7.3)$$

where *rect*$(\cdot)$ is a rectangle function and *Gauss*$(\cdot)$ is a Gaussian function as defined in [14].

Note in Eq. (7.3) and Fig. 7.2, the introduction of different scales x'', x', and x. The aperture in plane x'' is magnified at the scintillator plane, x', which is in turn magnified (or de-magnified) in the CCD plane, x. The aperture-to-scintillator magnification is given by $M_{\mathrm{D}} = d/L$, whereas the scintillator-to-CCD magnification is defined as $M_{\mathrm{CCD}} =$ *(object in scintillator plane/object in CCD sensor plane)*. The transformation, $x = M_{\mathrm{CCD}}x' = M_{\mathrm{D}}M_{\mathrm{CCD}}x''$, results in the following analytical model for the impulse response, h, at the CCD imaging plane, x,

$$h(x) = \mathrm{rect}\left(\frac{x}{M_{\mathrm{D}}M_{\mathrm{CCD}}D}\right) \times \mathrm{Gauss}\left(\frac{x}{M_{\mathrm{CCD}}\delta}\right) \times \mathrm{rect}\left(\frac{x}{\Delta s}\right) \quad . \qquad (7.4)$$

The normalized modulus of the Fourier transform of the impulse response is known as the modulation transfer function [7], defined as $MTF(u) = |H(u)|/|H(0)|$, where $H(u)$ is the system transfer function calculated by taking the Fourier transform of the impulse response. The MTF describes the magnitude of the frequency response of the system and is useful for depicting and quantifying system resolution as discussed in Chapter 6.

From Eq. 7.4, we can analytically produce $MTF(u)$ through Fourier transformation and simplification to yield,

$$MTF(u) = \left|\mathrm{sinc}\left(\frac{\mathrm{d}M_{\mathrm{CCD}}}{L/D}u\right) \cdot \mathrm{Gauss}(\delta M_{\mathrm{CCD}}u) \cdot \mathrm{sinc}(\Delta s\, u)\right| \quad , \qquad (7.5)$$

where $sinc(x) = sin(x)/x$. Note that this expression has been put into a form explicitly containing the L/D ratio.

In Eq. (7.5), the *sinc* $(\cdot)$ term drives much of the response typically observed in a radiography system. For example, as $L/D \rightarrow \infty$, this term broadens out in frequency representing improved resolution. Also, as the object moves closer to the detection plane, i.e., as $d \rightarrow 0$, resolution also improves. These are both effects that are readily observed in radiography systems.

An example of the MTF is shown on the left-hand-side of Fig. 7.3 for a system with the model parameters: $L/D = 150$, $d = 10$ cm, $\delta = 50$ μm, $\mathrm{M_{CCD}} = 0.25$. MTF is a measure of system response versus frequency content of the object being imaged. In this figure, the X axis represents frequency, with units of cycles per millimeter often referred to as line pairs per millimeter. The Y axis represents the transmission of this frequency to the image. In this example, the response to a sinusoid with 10 cyc/mm drops to approximately 55% of the sinusoid's amplitude.

Applying the Rayleigh criterion of 10% MTF [16] to this example, indicates that the highest resolvable frequency is 17 cyc/mm. System resolution is defined

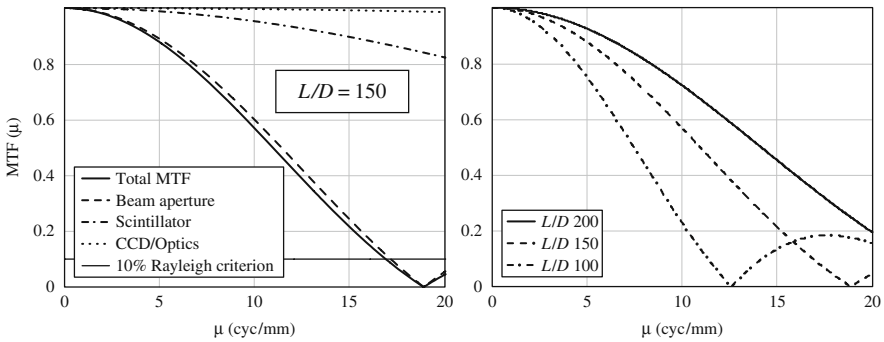

Fig. 7.3 MTF modeling results for typical radiography system parameters. The *left plot* shows the frequency response of constituent system components at a specified L/D ratio, while the *right plot* shows the system response for a variety of L/D ratios

as the period of this frequency. Therefore, resolution is $1/(17\ \text{cyc/mm}) = 60\ \mu\text{m}$ at the CCD imaging plane. Due to magnification in the system, the resolution at the object plane is 231 μm.

Note also for this geometry that the beam aperture (or equivalently the L/D ratio) is the primary factor impacting resolution. The scintillator screen and the optical system (defined by the CCD sample rate) produce only minor relative degradation. On the right-hand side of Fig. 7.3, the MTF is shown for a variety of L/D ratios, indicating the strong effect this factor has on the resolution of a neutron radiography system. Of course, the obvious result of this analysis is to increase the L/D ratio either by moving farther from the beam aperture or by reducing the size of the aperture. Unfortunately, both of these choices also result in a rapid reduction in the available neutron flux, requiring further signal-to-noise analysis to optimize both the geometry and the counting statistics.

7.2.2 System Performance Measurement

Measurement of system performance allows system designers to determine if the imaging system is performing as expected and to give potential users information useful in determining whether the imaging system is appropriate for their application. The key measurements of system performance are resolution and contrast discrimination. Resolution is a measure of the details that can be seen within an image while contrast discrimination measures the contrast required between an object and its background to resolve the object.

Resolution measurement methods can be categorized as direct and indirect. For direct methods, a series of test objects over a range of sizes near the resolution limits of the system are used. These test objects take many forms from line pairs to spheres to radial patterns and provide a direct visual display of the resolution on the radiographs [7].

Indirect resolution measurements use the edge response of the system to provide a more quantitative view of resolution. These measurements result in an MTF for the system. MTF can be calculated for radiography systems through measurement of the response of the system to an edge object. These edges are tilted to provide appropriate edge sampling by a pixilated imager [37, 32]. Tilted thin wires can also be used for this method [29]. The MTF is calculated from an edge image by first locating the edge within the radiograph and binning the edge response perpendicular to the line over the length of the line to get the edge response function, $E_{\mathrm{r}}(x)$. Taking a derivative of the edge response function produces the edge spread function, which is then Fourier transformed to produce $F(u)$, which is used to produce the MTF, where $F(u)$ is given explicitly by,

$$F(u) = \int E_{\mathrm{r}}'(x)\, \mathrm{e}^{-iux} dx \quad , \tag{7.6}$$

where $E_{\mathrm{r}}'(x) = dE(x)/dx$ represents a suitable discrete derivative process. Applying these methods to a radiograph will measure the MTF of the imaging system and verify the expected results based on the calculations from the previous section.

Neutron radiography systems are naturally extended to perform computed tomography (CT) for 3D reconstruction. Resolution of the reconstructed results will depend on the system, data collection, and reconstruction parameters as well as contrast in the object. Measurement of the empirical resolution of the 3D results after tomographic (CT) reconstruction can also be obtained from the determination of the edge response. The American Society for Testing and Materials (ASTM) has developed a standard test method for measurement of CT system performance designated E1695. In this standard, a cylindrical phantom is used to determine both spatial resolution and contrast discrimination measurements on the reconstructed data from a CT system as shown in Fig. 7.4. The shown example is a result from X-ray CT imaging; however, neutron tomography systems will produce the same type of data and the ASTM standard is directly applicable.

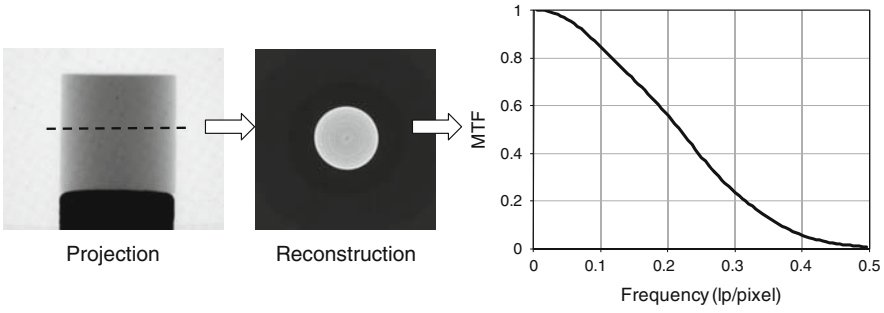

Fig. 7.4 Spatial resolution from CT reconstruction using ASTM E1695 standard

In the ASTM E1695 standard method, a cylindrical phantom is scanned and a slice normal to the central axis of the cylinder is reconstructed. A normal slice through the cylinder contains a circular cross-section of the cylinder. Just as in the tilted edge method, the MTF is calculated from the line edge response. The line edge response is found by locating the center of this circle and circularly integrating the pixels around this center point. In the tilted edge method, the tilt provides subpixel resolution across the edge. The pixel sampling on the circle edge will also provide this higher resolution edge response assuming the circle is of adequate size. Guidelines for the size selection are provided in the standard.

The MTF characterizes the spatial resolution of the system as described earlier. The second key performance parameter for CT systems is also included in ASTM E1965 and is the contrast discrimination function (CDF). The CDF measures the ability to discriminate an object from its background and is calculated using the same cylindrical phantom or spherical phantom used for the MTF calculation.

For calculation of the CDF, the region within the reconstructed slice through the phantom is subdivided into neighborhoods of size $N \times N$ as shown on the left side of Fig. 7.5. For CDF, the mean value for each neighborhood and the standard deviation of the means are calculated. This process is repeated for $N = 1,2,\ldots, M$, until there are fewer than 25 neighborhoods within the cylinder slice. Finally, for confidence in discrimination of the object from the background, the contrast needs to be three times greater than the standard deviation in the noise. Therefore, the standard deviations are multiplied by 3 and graphed as a function of neighborhood size to produce the CDF.

Since the cylinder is a uniform material, CDF can be interpreted as the average noise in the reconstructed image for various levels of pixelization. An example CDF is given on the right side of Fig. 7.5. In this example, the CDF shows that a contrast of 70% is required to discriminate a single pixel object from the background, and a contrast of 10% enables discrimination of objects larger than 3×3 pixels.

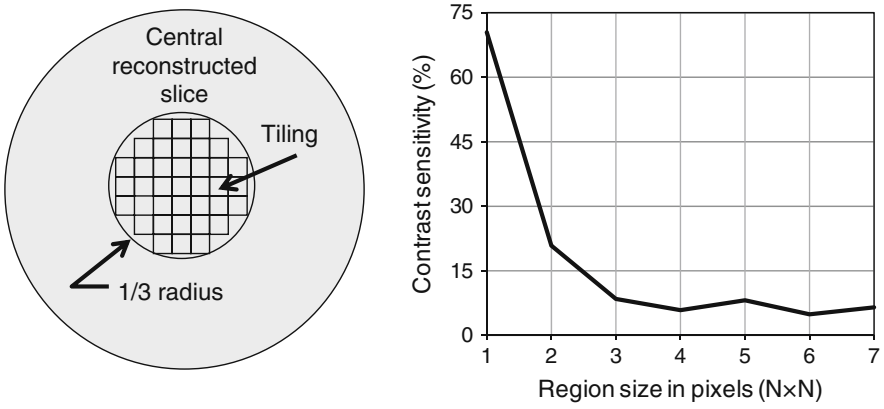

Fig. 7.5 Contrast discrimination measurement geometry (*left*) and CDF results (*right*)

The 3D MTF measurement method has been extended to use a spherical phantom [6] for two reasons. First, any tilt in the cylinder will produce an elliptical cross-section and degrade the calculated edge response, whereas any slice through a sphere will produce the appropriate circular cross-section. Second, resolution will vary over the reconstruction space for CT systems depending on the sampling and the reconstruction method used. This spherical phantom implementation locates the center of the sphere and integrates over spherical surfaces centered on this point to develop an edge response function that is an average over all directions on the spherical surface. Again using Eq. (7.6), the MTF is calculated over all directions.

With the resolution and contrast measurements presented in the graphical forms as shown in Figs. 7.4 and 7.5, a user can determine whether the imaging system is suited for a particular measurement.

7.3 Volumetric Imaging

Neutron imaging systems have followed the path of x-ray imaging systems in the introduction of rotational systems and CT reconstruction algorithms to perform volumetric imaging. An introduction to neutron tomography was provided in Chapter 6. This section builds upon the introduction by providing a mathematical description of CT and the classical methods for reconstruction of volumetric data.

Given a collection of projection images of an object, a 3D volumetric image can be reconstructed using either an analytic or an iterative algorithm. The former is based on some variant of filtered backprojection. The latter is based on optimization of a criterion function that relates the fit of the volumetric image with the observed projection data. In this section, we review the mathematics behind these conceptually different approaches and comment on advantages and disadvantages. To simplify the discussion, we apply the following model of the projection data:

$$I = I_0 \exp\left\{ - \int_K m(\alpha)\, d\alpha \right\} \quad , \tag{7.7}$$

where I_0 and I refer to the beam intensity before and after interaction with the object, K denotes the path of the beam, and m represents the material-dependent macroscopic cross-sections. To reconstruct m, which corresponds to Σ_T, in the preceding section for neutron radiography, we apply log-normalization to isolate the cross-section (Eq. (7.1), assuming B$\sim$1),

$$\int_K m(\alpha)\, d\alpha = -\log \frac{I}{I_0} \quad . \tag{7.8}$$

We note that in practice, the result of a dark field scan (where the source is turned off) is often subtracted from both I_0 and I to compensate for noise generated by physical processes that occur inside the imager (CCD).

Different imaging geometries require different reconstruction algorithms. We consider both parallel and divergent beam collimation of the neutron beam as shown in Fig. 7.6. We assume that the entire object is visible in each projection image and that it is placed on a turntable to allow for a circular orbit-type scan. Generalization to a helical scan is possible but beyond the scope of the present exposition.

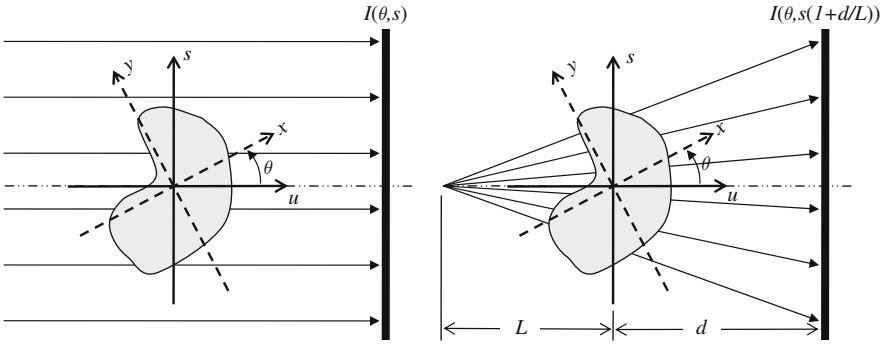

Fig. 7.6 Parallel beam (*left*) and fan beam (*right*) sampling geometries. Cone beam sampling extends the fan beam geometry axially

7.3.1 Filtered Backprojection

For 2D parallel beam data, the Fourier-slice theorem says that the Fourier transform of a 1D projection equals a comparably angled slice through the 2D Fourier space of the object being imaged [23]. Let $p\ (\theta,s)$ denote the log-normalized projection data and let $P\ (\theta,w)$ be the Fourier transform thereof. Mathematically,

$$\begin{aligned} p(\theta,s) &= \int_{-\infty}^{\infty} m(s\cos\theta - u\sin\theta, s\sin\theta + u\cos\theta)\, du \\ P(\theta,w) &= \int_{-\infty}^{\infty} p(\theta,s)\exp\{-i\,2\pi ws\}\, ds \end{aligned} \tag{7.9}$$

Merging these expressions, while introducing the variable substitutions $x = s\ cos\theta - u\ sin\theta$ and $y = s\ sin\theta + u\ cos\theta$, leads to,

$$\begin{aligned} P(\theta,w) &= \int\int_{-\infty}^{\infty} m(x,y)\exp\{-i2\pi\, w(x\cos\theta + y\sin\theta)\}dx\, dy \\ &= M(w\ \cos\ \theta, w\ \sin\ \theta) \end{aligned} \tag{7.10}$$

where M denotes the Fourier transform of m. While it would be tempting to superimpose appropriately rotated 1D Fourier transforms of a collection of projections and then obtain m through 2D Fourier inversion of the thus approximated version of M, the interpolation needed to map the radial data into the required Cartesian format would likely introduce artifacts in the resulting image.

Filtered backprojection is a better approach. The mathematical derivation can be summarized as follows [35]. When rewriting the inverse Fourier transform of M using polar coordinates, the resulting Jacobian introduces an absolute value-based frequency multiplier. That is,

$$\begin{aligned} m(x,y) &= \int\!\!\int_{-\infty}^{\infty} M(u,v)\ \exp\{i\,2\pi\,(ux+vy)\}\,du\,dv \\ &= \int_0^{\pi}\left[\int_{-\infty}^{\infty}|w|\,M(w\,\cos\theta, w\sin\theta)\exp\{\,i2\pi\,(x\,\cos\theta + y\,\sin\theta)\}\,dw\right] d\theta \end{aligned} \tag{7.11}$$

We can apply the Fourier-slice theorem to replace M (w cos θ, w sin θ) by P (θ,w). For simpler notation, we can furthermore express the inverse Fourier transform of $|w|$ P (θ,w) as a convolution of p (θ,s) with a kernel that implements the ramp-filter corresponding to $|w|$. The result is the well-known algorithm,

$$\begin{aligned} m(x,y) &= \int_0^{\pi} \tilde{p}(\theta, x\cos\theta + y\sin\theta)\,d\theta \\ \tilde{p}(\theta,s) &= p(\theta\,,s)\ \times\ h_{\mathrm{RAMP}}\,(s) \end{aligned} \tag{7.12}$$

where the ramp-filter is often band-limited to suppress high-frequency noise and sampling based aliasing.

The extension to a 2D fan-beam geometry is not difficult. Essentially, geometric weighting is introduced to compensate for the divergent nature of the projection rays. The algorithm for equiangular sampling seen in connection with a curved ring-detector is very similar to that associated with the equidistant sampling geometry of a linear detector. The latter algorithm is given by,

$$\begin{aligned} m(x,y,z) &= \frac{1}{2}\int_0^{2\pi} g^2(\theta,x,y)\tilde{p}(\theta, g(\theta,x,y)(x\cos\theta + y\sin\theta))\,d\theta \\ g(\theta,x,y) &= L/(L + x\sin\theta - y\cos\theta) \\ \tilde{p}(\theta,s) &= L/\sqrt{L^2+s^2}\cdot\ p(\theta,s)\times h_{\mathrm{RAMP}}\,(s) \end{aligned} \tag{7.13}$$

where L refers to the distance from the neutron beam aperture to the isocenter of the object (c.f. Fig. 7.6). The detector is assumed to be located at the isocenter for mathematical simplicity (i.e., $d=0$). Notice that the backprojection takes place over 2π instead of just π as used for the parallel beam geometry. Also note that $L\rightarrow\infty$ leads to the parallel beam algorithm.

The extension to 3D parallel beam data is even more straightforward. In fact, the reconstruction algorithm is identical to the one above for 2D parallel beam data except for the increase in dimensionality.

The extension to a 3D cone-beam geometry based on a flat-panel detector is more involved. Tuy [40] established a sufficient condition for reconstruction that says that every image plane must contain at least one source point. While this is satisfied for helical scanning and other trajectories, it is not satisfied for a circular-orbit scan, which is considered here. This leads to an approximate algorithm of which Feldkamp's without a doubt is the most widely used.

Developed for industrial x-ray cone-beam CT, the Feldkamp algorithm [13] can be viewed as a generalization of the fan-beam algorithm. The central slice of a cone-beam volume is reconstructed in exactly the same manner as it would have been, had it been reconstructed from single-slice fan-beam data. Slices further out in the cone, however, correspond to tilted fans and are thus handled differently. While the mathematical details are too extensive for inclusion here, the end result is the following algorithm,

$$\begin{aligned} m(x,y,z) &= \frac{1}{2}\int_0^{2\pi} g^2(\theta,x,y)\tilde{p}(\theta,g(\theta,x,y)[x\cos\theta + y\sin\theta, z])\,d\theta \\ g(\theta,x,y) &= L/(L + x\sin\theta - y\cos\theta) \\ \tilde{p}(\theta,[s,t]) &= L/\sqrt{L^2+s^2+t^2}\cdot p(\theta,[s,t]) \times h_{\mathrm{RAMP}}(s) \end{aligned} \tag{7.14}$$

Notice that $z=0$ leads to the fan-beam algorithm. Also note that filtering is not applied in the axial dimension.

We mentioned that the fan-beam backprojection equation indicates that the source trajectory data must cover 2π. However, by introducing a weight function that effectively limits each projection ray to be considered just once, Parker [34] showed that it is possible to stop when $\pi+\gamma$ has been covered where γ denotes the fan angle. The idea, which is heuristic, can be extended to apply to cone-beam data as well.

Filtered backprojection algorithms, whether exact or approximate, are based on continuous mathematics. When implemented for practical use, all integrals are replaced by Riemann sums and nonintegral projection data lookup indices are handled using some form of interpolation. The filtering can take place in either the spatial domain or the frequency domain. When based on fast fourier transforms, the latter can be done very efficiently. In that case, backprojection along with interpolation dominates the computational cost. Still, given recent advances in computer technology, it is possible to reconstruct even large images in a very short amount of time.

The image quality depends on taking enough projections and having good count statistics to work with. Not taking enough projections invariably leads to streak artifacts. Indeed, they are almost always present to some degree. Poor count statistics results in a low-contrast, grainy image. Under normal imaging conditions, however, good images are produced.

7.3.2 Iterative Reconstruction

Henceforth, let vectors $\mathbf{x}$ and $\mathbf{b}$ refer to the image representing the macroscopic cross-sections and the log-normalized projection data, and let matrix $\mathbf{A}$ denote the discretization of the projection integral connecting the two. Reconstruction can then be viewed as a matter of solving $\mathbf{Ax} = \mathbf{b}$. Numerous applicable iterative algorithms exist ranging from Gauss–Seidel, Jacobi, and other stationary methods to conjugate gradient (CG) and other Krylov subspace methods.

Stationary methods can be derived using matrix splitting [36]. For example, $\mathbf{A} = \mathbf{M} - \mathbf{N}$ leads to the iteration scheme,

$$\mathbf{x}^{(k+1)} = \mathbf{M}^{-1}\mathbf{N}\mathbf{x}^{(k)} + \mathbf{M}^{-1}\mathbf{b} \tag{7.15}$$

where $\mathbf{x}^{(0)}$ is given. Convergence to the desired solution is guaranteed if $\rho(\mathbf{M}^{-1}\mathbf{N}) < 1$ where ρ denotes the spectral radius of the matrix involved. Let matrices $\mathbf{D}$, $\mathbf{L}$, and $\mathbf{U}$ represent the diagonal, strictly lower triangular, and strictly upper triangular portions of $\mathbf{A}$. Then Gauss–Seidel is the result of setting $\mathbf{M} = \mathbf{D} - \mathbf{L}$ and $\mathbf{N} = \mathbf{U}$. Likewise, Jacobi follows from setting $\mathbf{M} = \mathbf{D}$ and $\mathbf{N} = \mathbf{L} + \mathbf{U}$. Both methods converge if $\mathbf{A}$ is strictly diagonally dominant.

Krylov subspace methods monotonically minimize the residual error using orthogonality conditions [36]. They are nonstationary in the sense that the computations involve information that changes each iteration. The prototypical example is CG, which is based on the assumption that matrix $\mathbf{A}$ is symmetric, positive-definite. The iterative update scheme is given by

$$\begin{aligned}
\alpha &= |\mathbf{r}^{(\mathrm{k})}|^2 / |\mathbf{d}^{(\mathrm{k})}|_{\mathrm{A}}^2 \\
\mathbf{x}^{(\mathrm{k}+1)} &= \mathbf{x}^{(\mathrm{k})} + \alpha\, \mathbf{d}^{(\mathrm{k})} \\
\mathbf{r}^{(\mathrm{k}+1)} &= \mathbf{b} - \mathbf{A}\mathbf{x}^{(\mathrm{k}+1)} \\
\beta &= |\mathbf{r}^{(\mathrm{k}+1)}|^2 / |\mathbf{r}^{(\mathrm{k})}|^2 \\
\mathbf{d}^{(\mathrm{k}+1)} &= \mathbf{r}^{(\mathrm{k})} + \beta\, \mathrm{d}^{(\mathrm{k})}
\end{aligned} \tag{7.16}$$

where $\mathbf{x}^{(0)}$ is given, $\mathbf{d}^{(0)} = \mathbf{r}^{(0)} = \mathbf{b} - \mathbf{A}\mathbf{x}^{(0)}$, $|\mathbf{r}|^2 = \mathbf{r}^{\mathrm{T}}\mathbf{r}$, and $|\mathbf{d}|_{\mathrm{A}}{}^2 = \mathbf{d}^{\mathrm{T}}\mathbf{A}\mathbf{d}$.

Whether a stationary method or a Krylov subspace method is used, the search for $\mathbf{x}$ is terminated either when the residual norm associated with the current iterate is deemed to be small enough, or when a fixed number of iterations have been executed.

In most imaging applications, the linear system is under-or overdetermined and a least squares problem must be solved instead. Let this be denoted by

$$\mathbf{x}^* = \mathrm{argmin}|\mathbf{Ax} - \mathbf{b}|^2 \quad , \tag{7.17}$$

where $|\mathbf{Ax}-\mathbf{b}|^2 = (\mathbf{Ax}-\mathbf{b})^{\mathrm{T}}(\mathbf{Ax}-\mathbf{b})$. By taking the derivative of the squared residual norm with respect to $\mathbf{x}$ and equating the result to zero, we obtain the

normal equations which form a linear system that can be solved by any of the above-mentioned methods, namely,

$$\mathbf{A}^{\mathrm{T}}\mathbf{A}\mathbf{x} = \mathbf{A}^{\mathrm{T}}\mathbf{b} \tag{7.18}$$

Other methods include SIRT, which is a stationary method for solving a weighted least squares problem that has been widely used in medicine and biology [15;18]) and LSQR, which is a CG-like method with better numerical properties [33].

The reconstructed image should not contain any negative values, as they have no physical interpretation. Their absence is only guaranteed if the least squares problem is constrained accordingly. This leads to,

$$\mathbf{x}^* = \mathrm{argmin}|\mathbf{A}\mathbf{x} - \mathbf{b}|^2 \mathrm{subject\ to}\, \mathbf{x} \geq 0 \quad . \tag{7.19}$$

Note that depending on the neutron imaging system, a highly scattering object can cause neutron detection in detectors just outside the shadow of the object under test. These additional neutrons can result in negative attenuation values. Therefore, modifications to the typical constraints may be required along these edges.

A number of methods exist for solving constrained quadratic optimization problems, one example being to embed the least squares algorithm in a projected gradient framework [5, 19]. Computationally, an outer algorithmic layer iteratively (i) uses an inexact line search based on safeguarded quadratic interpolation to determine the set of free variables, i.e., those that are strictly positive and (ii) invokes the least squares algorithm to compute a feasible solution in that subspace. Control is passed back from the least squares solver to the outer algorithmic layer either at convergence or when a variable is about to violate the nonnegativity constraint.

Computational steering can be introduced through the addition of a penalty term [26]. For example, suppose that the image is known to consist of regions of uniform macroscopic cross-sections. In that case, it might be advantageous to discourage neighboring voxels from taking on different values except near region boundaries. This could be achieved by applying an edge-preserving Markov random field that has smoothing properties [8]. Other structural constraints are possible. Generally speaking, the resulting optimization problem can be written as

$$\mathbf{x}^* = \mathrm{argmin}|\mathbf{A}\mathbf{x} - \mathbf{b}|^2 + \beta\, \mathrm{R}(\mathbf{x}) \text{ subject to } \mathbf{x} \geq 0 \tag{7.20}$$

where $\mathrm{R}(\mathbf{x})$ denotes the penalty term and β is a free parameter that controls the influence exerted thereby on the solution. From a computational point of view, linear penalty terms are preferable as they can be handled by straightforward row-expansion of $\mathbf{A}$ and $\mathbf{b}$.

Bayesian reconstruction forms an alternative to algebraic methods. Commonly used in the field of medical imaging, this iterative approach is statistical by nature. The image formation is described probabilistically, thereby making reconstruction a matter of model parameter estimation. Specifically, let $p(\mathbf{x},\mathbf{b}|\Omega)$ denote the data likelihood for **x,** the unobservable image data, and **b,** the observable projection data, given Ω, the associated model parameters. As above, $\mathbf{Ax} = \mathbf{b}$, only now **A** is a matrix of detection probabilities. The goal is then to solve the penalized maximum likelihood problem

$$\Omega^* = \text{argmax log } p(\mathbf{x}, \mathbf{b}|\Omega) + \beta R(\Omega) \quad . \tag{7.21}$$

where **R,** strictly speaking, is a log-prior; although in practice a heuristic smoothing term is often used.

Methods for maximum likelihood estimation include gradient descent, conjugate gradient, and similar algorithms. These typically require first and/or second derivatives of the likelihood function to be evaluated. This is not the case for the two-step EM algorithm [11]. First, an E-step is carried out to compute the expectation of the data log-likelihood given the observed data and the current parameter estimate. Then, an M-step is used to re-estimate the model parameters by means of maximization of the expectation. The result is the following iteration scheme

$$\Omega^{k+1} = \text{argmax } E[\log p(\mathbf{x}, \mathbf{b}|\Omega)|\mathbf{b}, \Omega^{(k)}] + \beta R(\Omega) \tag{7.22}$$

In some applications, e.g., maximum likelihood estimation for independent Poisson events, the M-step is trivial as it has a closed-form solution. This allows the E-step and the M-step to be combined. For other applications, the M-step has to be implemented as an iterative computation of its own. This may also be the case for penalized maximum likelihood estimation, as the penalty term may preclude true maximization from taking place. The M-step is then turned into an iterative parameter update computation that ensures a nondecrease of the likelihood [21].

There are several advantages associated with taking an iterative approach to image reconstruction. For one, it is possible to quite accurately model the system geometry including nonuniformities in the sampling pattern as well as sensitivity variations across the detector. As pointed out above, it is also possible to steer the computation away from structurally undesirable images. Poor count statistics tend not to be a problem either, as the objective of both algebraic and statistical reconstruction methods is to find a solution that best fits the data. That is, there is no built-in assumption of data consistency across projections. Iterative approaches also allow reconstruction with few projections and irregular projection patterns and enable the inclusion of more accurate physics models up to full Monte Carlo models. This flexibility comes at a high cost with respect to both implementation complexity and computational cost at run-time. However, if these can be overcome, the payoff is a high-quality image.

7.3.3 Computer Platforms

Many platforms exist that can provide the compute power needed in order for a volumetric image to be reconstructed in a reasonable amount of time. A relatively small cluster of multi-core PCs may suffice to solve even a rather large problem in a matter of minutes [18]. From a programming point of view this is conceptually straightforward as it merely involves writing multi-threaded code for a distributed memory environment. In recent years, commodity graphics processing units (GPUs) have seen a rapid increase in both capability and programmability to the point that they are now being used for general purpose computing and thus also tomographic image reconstruction [31]. Papers often report order-of-magnitude performance gains over optimized CPU applications. However, GPU programming is not for the novice. Also, floating-point arithmetic may not follow IEEE standards, which could be a problem. Field-programmable gate-arrays (FPGAs) provide a different but equally powerful platform from a data throughput point of view. However, FPGAs are notoriously difficult to program, especially since floating-point arithmetic may not be supported to the extent needed. Finally, we mention the cell processor, which conceptually is somewhat similar to a multi-core CPU only orders-of-magnitude faster. High-level programming is possible, e.g., in C, but some thought must be devoted to memory handling as the processing units only have a limited amount of memory available. Nonetheless, the cell may represent the fastest platform currently on the market for volumetric imaging [22].

7.4 Conclusions and Application

The ability to model, design, and measure the resolving power of a radiography system is critically important to the experimental design required to achieve relevant measurement characteristics of complex, material structures. The focus of this chapter has been on methods to design and characterize radiography systems according to experimental goals for volumetric measurements (i.e., CT recording and reconstruction methods). This focus has been primarily related to spatial resolution and the estimation of macroscopic material interaction cross-sections.

New or modified radiography facilities that generate cold neutrons [38] provide wavelength tunable monochromaters [39] or provide time-of-flight (TOF) measurements [27], facilitating the radiographic capture of images that take $I(\theta,\Sigma_T,x,y,z)$ to $I(E,\theta,\Sigma_T,t,x,y,z)$. The ability to better characterize the energy–time–space dependencies of materials, $\Sigma_T(E,t,x,y,z)$, will produce better material resolution.

As an example of how to adapt this discussion to higher resolution measurements, consider the example MTF shown in Fig. 7.7. Using Eq. (7.5), we have

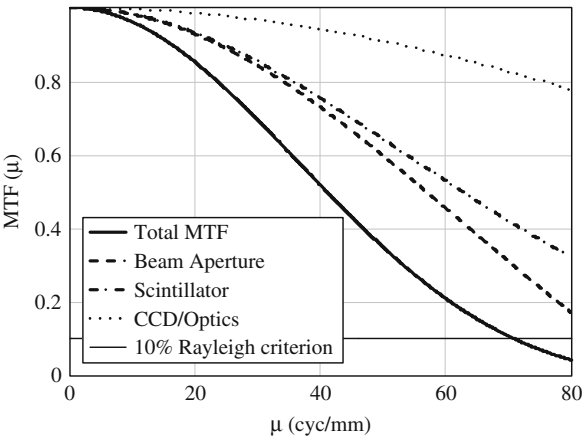

Fig. 7.7 MTF for a system design with $L/D = 750$, corresponding to an aperture size of 5 mm. the resolution (71 cyc/mm or 14 μm at the detector) is now comparable to the scintillator limit. How do we achieve sufficient neutron counting statistics?

hypothesized a radiography system with $L/D = 750$, corresponding to a beam aperture of 5 mm at a distance of 3.75 m from the object—a seemingly achievable design. For a scintillator material with an optical diffusion parameter of $\sigma = 10$ μm, the resolution of such a system would be 14 μm at the sensor, moving from the macro-analysis scale to the microscopy scale. Reducing the beam aperture from 25 mm (our earlier example) to 5 mm will increase system resolution by a factor of 4, yet it is likely that neutron-counting statistics and background noise will result in measurement challenges that are difficult to overcome.

Overcoming low neutron counts may be achievable by encoding the beam aperture, i.e., implementing an array of 5×5 mm (or smaller) apertures that constitute a significant total area (e.g., $>25 \times 25$ mm). In such a case, the MTF of Eq. (7.5) could be replaced by a new geometric transfer function, $H_{\mathrm{CA}}(\cdot)$ that describes a coded aperture [17], e.g.,

$$MTF(u) = \left| H_{\mathrm{CA}}\left(\frac{\mathrm{d}\,\mathrm{M}_{\mathrm{CCD}}}{L/D}u\right) \cdot Gauss(\sigma\, M_{\mathrm{CCD}}u) \cdot \sin c(\Delta s\, u)\right| \qquad (7.23)$$

The point is that these analysis tools can be adapted to new, more stringent resolution requirements by applying creative ideas and methods.

For another example, the steady-state flux of a conventional reactor cannot readily interrogate time-dependent phenomena as deeply as the high-intensity and energy-dependent beams available at a spallation neutron source. Using a spallation source, the potential exists to develop new time-synchronized, energy-resolved methods to better resolve subtle material differences. This is potentially achievable by taking advantage of the Bragg edges in materials [27] or of the fact that absorption cross-sections, σ_{a} at low neutron energies are typically proportional to $1/\sqrt{\mathrm{E}}$. Using prior knowledge of the material characteristics under test should facilitate the collection of a series of

energy-windowed images, $I_{\Delta E}(\theta,\Sigma_T,x,y,z)$, whose linear combinations, e.g., using principle component or linear discriminant analysis [12], may provide improved contrast (i.e., CDF) between materials.

Finally, any of these methods that compartmentalize the total neutron beam into small spatial- or energy-dependent units will make volumetric recovery of material characteristics more challenging due to reduced signal-to-noise and the corresponding artifacts that conventional CT methods produce in low-signal environments. In these situations, the iterative reconstruction methods introduced in Section 7.3.2 become more relevant to achieving adequate signal recovery and reconstruction.

References

1. R. Accorsi, F. Gasparini, et al., A Coded aperture for high-resolution nuclear medicine imaging with conventional anger camera. *IEEE Trans. Nucl. Sci.* **48**:6, 2411 (2001).
2. H. Asano, N. Takenaka, et al., Visualization and void fraction measurement of gas-liquid two-phase flow in a commercial plate heat exchanger by thermal neutron radiography. *IEEE Trans. Nucl. Sci.* **52**:1, 280–284 (2005).
3. M. Balasko, E. Svab, et al., Comparison of neutron radiography with other nondestructive methods. *IEEE Trans. Nucl. Sci.* **52**:1, 330–333 (2005).
4. L.G.I. Bennett, T.R. Chalovich, et al., Comparison of neutron radiography with other non-destructive techniques for the inspection of cf188 flight control surfaces. *IEEE Trans. Nucl. Sci.* **52**:1, 334–337 (2005).
5. M. Bierlaire, P.L. Toint, et al., On iterative algorithms for linear least squares problems with bound constraints. *Linear Algebra Appl.* **143,** 111–143 (1991).
6. P. Bingham, L. Arrowood, et al., Calibration and performance testing for reconfigurable computed tomography systems. *Mat. Eval.* **65,** 1102–1107 (2007).
7. G.D. Boreman, *Modulation Transfer Function in Optical and Electro-Optical Systems*. Bellingham, WA, SPIE Press (2001).
8. C.Bouman and K. Sauer, A generalized Gaussian image model for edge-preserving MAP estimation. *IEEE Trans. Image Process.* **2**, 296–310 (1993).
9. S. Casalta, G.G. Dawuino et al., Digital image analysis of X-ray and neutron radiography for the inspection and the monitoring of nuclear materials. *NDT&E Int.* **36**, 349–355 (2003).
10. J.M. Cimbala, J.S. Brenizer, et al., Study of a loop heat pipe using neutron radiography. *Appl. Radiat. Isot.* **61**, 701–705 (2004).
11. A. Dempster, N. Laird, et al., Maximum likelihood from incomplete data via the EM algorithm. *J. R. Stat. Soc. B* **39**, 1–38 (1977).
12. R.O. Duda, P.E. Hart, et al., *Patt. Class.*. New York, John Wiley & Sons, Inc. (2001).
13. L.A. Feldkamp, L.C. Davis, et al., Practical cone beam algorithm. *J. Opt. Soc. Am. A* **1**, 612–619 (1984).
14. J.D. Gaskill, *Linear Systems, Fourier Transforms, and Optics*, John Wiley & Sons, Inc. (1978).
15. P. Gilbert, Iterative methods for the three-dimensional reconstruction of an object from projections. *J. Theor. Biol.* **36**, 105–117 (1972).
16. J.W. Goodman, *Introduction to Fourier Optics*, Roberts & Company Publishers (2004).
17. S.R. Gottesman, and E.E. Fenimore, New family of binary arrays for coded aperture imaging. *Appl. Opt.* **28**:20, 4344 (1989).
18. J. Gregor and T. Benson, Computational analysis and improvement of SIRT. *IEEE Trans. Med. Imaging* **27**, 918–924 (2008).

19. J. Gregor and F.R. Rannou, *Least squares framework for projection MRI reconstruction*. Medical Imaging, San Diego, CA, Proceedings of SPIE (2001).
20. A.A. Harms and D.R. Wyman, *Mathematics and Physics of Neutron Radiography*. Boston, D. Reidel Publishing Company (1986).
21. T. Hebert and R. Leahy, A generalized EM algorithm for 3-D Bayesian reconstruction from Poisson data using Gibbs priors. *IEEE Trans. Med. Imaging* **8**, 194–202 (1989).
22. M. Kachelriess, M. Knaupp, et al., Hyperfast parallel-beam and cone-beam backprojection using the Cell general purpose hardware. *Med. Phys.* **34**, 1471–1486 (2007).
23. A. Kak and M. Slaney. *Principles of Computerized Tomographic Imaging*, IEEE Press (1988).
24. G.F. Knoll, *Radiation Detection and Measurement*, John Wiley & Sons, Inc. (2000).
25. J.R. Lamarsh, *Introduction to Nuclear Engineering*, Addison-Wesley Publishing Company (1983).
26. C.L. Lawson and R.J. Hanson, *Solving Least Squares Problems*, Prentice-Hall (1974).
27. E. Lehmann, P. Vontobel, et al., Neutron imaging – present status and options with tof methods – TOF neutron imaging. *J. Neutron Res.* **13**, 27–31 (2005).
28. U. Matsushima, Y. Kawabata, et al., Measurement of changes in water thickness in plant materials using very low-energy neutron radiography. *Nucl. Instrum. Meth. Phys. Res. A* **542**, 76–80 (2005).
29. S.L. Meeks, J.F. Hamon, et al., Performance characterization of megavoltage computed tomography imaging on a helical tomotherapy unit. *Med. Phys.* **32**, 2673–81 (2005).
30. J.J. Milczarek, A. Czachor, et al., Dynamic neutron radiography observations of water migration in porous media. *Nucl. Instrum. Meth. Phys. Res. A* **542**, 232–236 (2005).
31. K. Müller and F. Xu, Accelerating popular tomographic reconstruction algorithms on commodity PC graphics hardware. *IEEE Trans. Nucl. Sci.* **3,** 654–663 (2005).
32. M. Ohkubo, S. Wada, et al., An effective method to verify line and point spread functions measured in computed tomography. *Med. Phys.* **33**, 2757–64 (2006).
33. C.C. Paige and M.A. Saunders, LSQR: An algorithm for sparse linear equations and sparse least squares. *ACM Trans. Math. Software* **8**, 43–71 (1982).
34. D. Parker, Optimal short-scan convolution reconstruction for fanbeam CT. *Med. Phys.* **9**, 254–257 (1982).
35. A. Rosenfeld and A. Kak, *Digital Picture Processing*, Academic Press (1976).
36. Y. Saad, *Iterative Methods for Sparse Linear Systems*, PWS Publishing Co (1996).
37. E. Samei and M.J. Flynn, A method for measuring the presampled MTF of digital radiographic systems using an edge test device. *Med. Phys.* **25,** 102–113 (1998).
38. M. Tamaki, Conceptual monochromatic digital neutron radiography using continuous cold neutron beam. *Nucl. Instrum. Meth. Phys. Res. A* **542,** 32–37 (2005).
39. W. Treimer, M. Strobl, et al., Wavelength tunable device for neutron radiography and tomography. *Appl. Phys. Lett.* **89,** 203504 (2006).
40. H. Tuy, An inversion formula for cone-beam reconstruction. *SIAM J. Appl. Math.* **43,** 546–552 (1983).